



CHORUS

This is the accepted manuscript made available via CHORUS. The article has been published as:

Photoelectron energy spectra from elastic rescattering in ultrastrong laser fields: A relativistic extension of the three-step model

S. S. Luo, P. D. Grugan, and B. C. Walker

Phys. Rev. A **91**, 033412 — Published 26 March 2015

DOI: [10.1103/PhysRevA.91.033412](https://doi.org/10.1103/PhysRevA.91.033412)

Photoelectron Energy Spectra from Elastic Rescattering in Ultrastrong Laser Fields: A Relativistic Extension of the Three-Step Model.

S.S. Luo, P.D. Grugan, and B.C. Walker

Department of Physics and Astronomy,

University of Delaware, Newark, DE 19716, USA

(Dated: March 5, 2015)

Abstract

Using a relativistic adaptation of a three-step recollision model we calculate photoelectron energy spectra for ionization with elastic scattering in ultrastrong laser fields up to 24 a.u. (2×10^{19} W/cm²). Hydrogen-like and noble gas species with Hartree-Fock scattering potentials show a reduction in elastic rescattering beyond 6×10^{16} W/cm² when the laser Lorentz deflection of the photoelectron exceeds its wave function spread. A relativistic rescattering enhancement occurs at 2×10^{18} W/cm², commensurate with the relativistic motion of a classical electron in a single field cycle. The noble gas results are compared with available experiments. The theory approach is well suited to modeling scattering in the ultrastrong intensity regime that lies between traditional strong fields and extreme relativistic interactions.

I. INTRODUCTION

High strength laser fields can ionize the outer, least tightly bound electron from atoms and molecules by overcoming the binding nuclear Coulomb field. Fields of this strength (0.17 a.u., intensities of 10^{15} W/cm²) also dominate photoelectron dynamics and the oscillating laser field can force the photoelectron to return and ‘rescatter’ with the parent ion [1]. Over the past twenty years, strong field ionization and rescattering has been used to measure electron dynamics [2], collisionally excite multiple electrons [3], generate coherent attosecond x-ray light [4], and perform molecular tomography [5]. For optical frequency lasers, these phenomena occur on energy scales (e.g. the ponderomotive [1] or ‘quiver’ energy $U_p = e^2|E|^2/(4m\omega^2)$ for an electron charge $-e$ in an oscillating electric field E , frequency ω) that are less than one-percent of the electron rest mass, m . Hence, the interaction is safely described nonrelativistically using the dipole approximation, $\vec{E} \cdot \vec{r}$ in the length gauge. Models for these interactions [6–11] range from fully quantum one-electron [12] or multi-electron treatments [13] to insightful one-electron [14] and multi-electron classical theories [15, 16].

When the laser field is increased, more tightly bound electrons ionize; up to twenty-six electrons have been ionized for 24 a.u. laser fields (2×10^{19} W/cm²) [17]. In these ultrastrong fields, relativistic dynamics [18] are important and photoelectron energies can exceed several times the electron rest mass [19]. The laser field may no longer be simply approximated and the laser magnetic field B is required [20]. Research with mid-IR wavelength lasers and kiloelectron volt energy attosecond XUV pulses are also beginning to venture into the ultrastrong field frontier [21]. Theoretical underpinnings common to strong field models fail in ultrastrong fields. New approaches are required to overcome the numerous challenges such as three dimensional spatial dynamics that extend relativistically from an atomic unit of length to that of an optical wavelength in a femtosecond. Theory treatments have ranged from one-electron time dependent Dirac and Klein-Gordon solutions [22] to fully classical [23–26]. Recent calculations have addressed the fundamental physics including the role of electron spin [27]. At this time, the theoretical approaches have reached a point where it is possible to compare with experimental results in a quantitative way. Such comparisons will make it possible to identify complex dynamics and multi-electron physics.

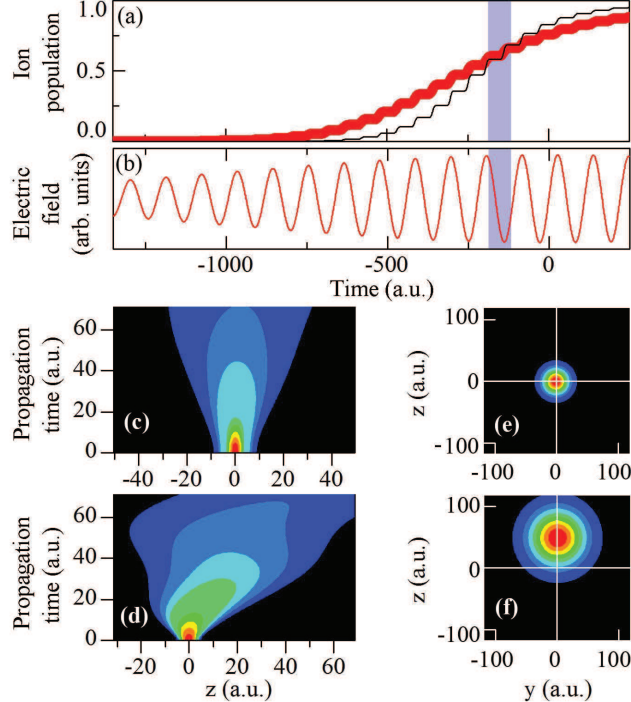


FIG. 1. (color online) He^+ (bold) and Ar^{8+} (thin) population (a) as a function of time in the laser field (b) whose peak intensity is $2.4 \times 10^{15} \text{ W/cm}^2$ for He^+ and 5.2×10^{16} for Ar^{8+} . The shaded region from -188 a.u. to -116 a.u. (a,b) indicates the time from ionization to scattering return for (c,d). The continuum electron density along z during this 72 a.u. window is shown for He^+ (c) and Ar^{8+} (d). The y - z flux profile at return is shown for He^+ (e) and Ar^{8+} (f).

II. RELATIVISTIC, THREE-STEP RECOLLISION MODEL

An emerging technique which accurately captures much of the physics and can be useful when comparing to experimental results involves treating interactions such as ionization [28] or radiation [29] quantum mechanically and propagation of the photoelectron in the field classically when the electron deBroglie wavelength is much smaller than the drive wavelength. Ionization and propagation components of this model compare favorably with recent ultrastrong field experiments [31]. Monte-Carlo trajectory ensembles in the model capture essential quantum aspects of the electron [32, 33] and such semiclassical approaches have been compared to full quantum solutions with the Dirac equation [34]. Adding elastic rescattering is a natural extension of the model and the approach has advantages in its connection to the well known three step model [30]. Perhaps more important is the ability to include temporal and spatial integrated experimental conditions. Relativistic dynamics

and a focal geometry inherent to all ultrastrong field experiments lead to complicated field accelerations that depend on the position and time in the laser field. Rendering a result for comparison to experimental result has involved, for example [31], spatial integration over 10^{-3} meter distances and 10^{-13} seconds. There is also a natural extension of the technique to plasma physics in ultrastrong fields, which utilizes classical particle-in-cell methods.

We report photoionization and fully relativistic elastic scattering [36] in ultrastrong fields. Key questions addressed include the final photoelectron energies as they are affected by elastic rescattering [35], atomic scattering potentials, the laser magnetic field, and relativistic effects. The work helps quantify the changes in rescattering as one moves from the strong field to ultrastrong field. After the ionization process itself, elastic scattering is the primary mechanism by which the field energy is transferred to atomic and ion systems. Using hydrogen-like and screened atomic scattering potentials for noble gas species, we are able to model elastic rescattering as a function of intensity. Magnetic deflection effects [20] are observed beyond 6×10^{16} W/cm² when the rescattering parameter [37] ($\Gamma_r = U_p^{3/2} V_{IP}^{1/2} / (3c^2 \omega)$ for ionization from a binding energy V_{IP}) indicates the Lorentz deflection of the photoelectron equals its wave function spread. Relativistic scattering enhancements are observed for intensities beyond 2×10^{18} W/cm² where the classical field nonlinearity parameter ($a_0 = e|E|/(\omega mc)$) signifies the electron motion is relativistic within a single field cycle. The extreme relativistic regime ($a_0 > 10$) [18] lies beyond the scope of this work. Lasers that promise to achieve extreme relativistic intensities [38] are under construction. Atomic units are used throughout the work except as noted where conventional units (e.g. W/cm²) are used for comparison to other work.

A. Ionization

Our calculations use linearly polarized light, $\vec{E} = E_0 \sin(kz - \omega t) \exp(-(t - z/c)^2/\sigma^2) \hat{x}$, with a pulse duration $\sigma = 34$ fs and carrier wavelength $\lambda = 2\pi/k = 800$ nm. When considering the full field $\vec{B} = |E|/c \hat{y}$. In the dipole approximation we set $\vec{B} = 0$. This plane wave is used for all cases except as noted for comparison with data at 10^{19} W/cm² where we adopt the experimental focus. Ionization is calculated using the ADK rate [39] for hydrogen-like 1s states and least tightly bound electron for the noble gas ions. The ionization curves for He⁺ and Ar⁸⁺ are shown in Fig. 1 along with the laser electric field.

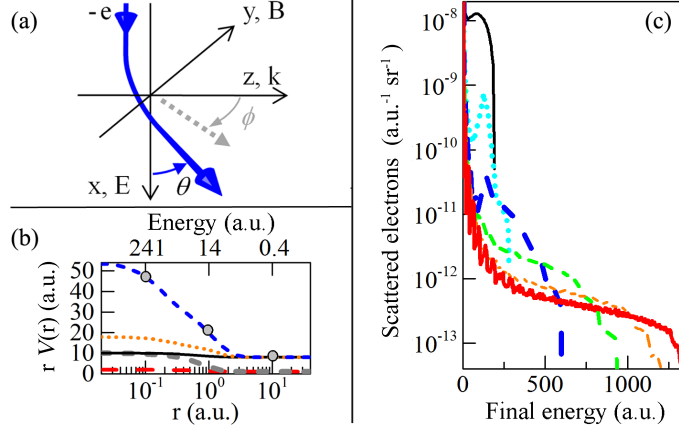


FIG. 2. (color online) Coordinate system (a) for scattering with the parent ion (origin). The scattering potentials (plotted as effective charge in atomic units $rV(r)$ as a function of r) are shown in (b) for Xe^{8+} (dash, blue), Ar^{8+} (dotted, orange), Ne^{8+} (solid, black), Ne^+ (thick dash, gray), and He^+ (long dash, red). For Xe^{8+} the energy corresponding to the minimum r and effective charge for $\theta = \pi/2$ scattering is indicated by the top axis and on the Xe^{8+} potential curve (circle, filled gray). Energy and angle (θ) resolved scattering (c) from hydrogen-like ($Z = 3$) at 6×10^{16} W/cm^2 for $0.05 < \theta < 0.5$ (solid black), $0.5 < \theta < 1.0$ (dotted, light blue), $1.0 < \theta < 1.55$ (long dash, blue), $1.55 < \theta < 2.1$ (dash, green), $2.1 < \theta < 2.6$ (short dash, orange), and $2.6 < \theta < 3.14$ (thick solid, red).

To keep the comparisons across species similar, E_0 is chosen so that ionization reaches 90% by the end of the pulse. Such a treatment of ionization rate is believed to be accurate within a factor of two. Relativistic and Coulomb factors [40] lead to corrections in the rate of less than 25% for the cases presented here.

B. Continuum Dynamics

After ionization, a Gaussian Monte-Carlo ensemble electron ‘wave packet’ is launched in the continuum with a quantum spread from the initial ionization width [37] and subsequent propagation. The deflection due to B is calculated using the Lorentz force on the photoelectron, $\vec{F} = -e\vec{E} - e\vec{v} \times \vec{B}$. As the electron interacts with a soft core potential, $\frac{Ze}{\sqrt{r^2 + \delta}}$, and external field, the position and momenta for the trajectories within the Monte-Carlo

ensembles are generated by integrating Hamilton's equations of motion:

$$\frac{dp_x}{dt} = \frac{-Ze^2x}{(r^2 + \delta)^{3/2}} - eE_x \left[1 - \frac{p_z}{\sqrt{p^2 + m^2c^2}} \right] \quad (1)$$

$$\frac{dp_y}{dt} = \frac{-Ze^2y}{(r^2 + \delta)^{3/2}} \quad (2)$$

$$\frac{dp_z}{dt} = \frac{-Ze^2z}{(r^2 + \delta)^{3/2}} - \frac{eE_x p_x}{\sqrt{p^2 + m^2c^2}} \quad (3)$$

$$\frac{dx}{dt} = \frac{p_x c}{\sqrt{p^2 + m^2c^2}} \quad (4)$$

$$\frac{dy}{dt} = \frac{p_y c}{\sqrt{p^2 + m^2c^2}} \quad (5)$$

$$\frac{dz}{dt} = \frac{p_z c}{\sqrt{p^2 + m^2c^2}} \quad (6)$$

Where c is the speed of light, δ is the soft core parameter (typically $\delta = 0.5$), Z is the atomic number, $r = \sqrt{x^2 + y^2 + z^2}$ and $p = \sqrt{p_x^2 + p_y^2 + p_z^2}$. When only the dipole approximation is considered, the Lorentz force terms from B are zero, resulting in $p_z/\sqrt{p^2 + m^2c^2}$ in equation (1) and E in equation (3) being dropped. For most calculations, the soft core potential term is set to zero since, as we will show, it does not affect the results presented here.

Also shown in Fig. 1(c, d) is an example rescattering flux 'snapshot' from a collection of electron trajectories for He^+ and Ar^{8+} with the ionization and return scattering time indicated in Fig. 1(a,b). Strong field rescattering (Fig. 1(c)) shows the traditional spreading and return of the electron after ionization while for ultrastrong field rescattering (Fig. 1(d)) the Lorentz deflection acts to displace the electron by ~ 50 a.u. along z . The > 20 a.u. spatial extent of the returning electron justifies a plane-wave approximation. Compared to ionization of neutrals or molecules, the plane wave approximation becomes more accurate for ionization in ultrastrong fields. The smaller extent of more tightly bound states results in a greater spreading of the ionized electron due to the uncertainty principle. This increase in spreading is evident when comparing the ionization of Ar^{8+} in Fig. 1(f) to that of He^+ in Fig. 1(c). With regard to the use of trajectory ensembles in the continuum, the deBroglie wavelength of the continuum electron is typical 0.5 to 0.01 atomic units of length.

C. Elastic Rescattering

Upon revisiting the parent ion, elastic scattering is calculated using a full partial-wave calculation [41]. Elastic scattering (Fig. 2) is calculated for hydrogen-like species using a

bare nucleus, Coulomb potential, $V(r) = Ze/r$. Low energy scattering with unphysically large impact parameters (given the finite extent of the electron) is avoided by eliminating scattering energies below $0.3 U_p$. Neglecting these energies does not affect final state results above $0.3 U_p$. For noble gases, we use Hartree-Fock screening of the nucleus with a screening charge density given by, $\rho_e(r) = \frac{Ze}{4\pi r} \sum_{i=1}^3 D_i d_i^2 \exp^{-d_i r}$, with the D_i and d_i coefficients calculated using the ELSEPA routine [41]. The charge distribution ρ_e is used to obtain the screening potential from which scattering is calculated. While the scattering charge for hydrogen-like species is independent of r , atomic species have an effective charge that depends on the distance from the nucleus due to screening. The effective charge for scattering with Xe^{8+} is 8 for relatively large $r = 4$ a.u., increasing to 20 for an interaction at $r = 1$ a.u., and to 47 (nearly the full value of the bare nucleus) at $r = 0.1$ a.u. For $\theta = \pi/2$ scattering, the incident energies corresponding to these impact parameter distances are shown in the Fig. 2(b) top x-axis. Impact parameter distances of $r = 1$ a.u. have an incident energy of 14 a.u. for $\theta = \pi/2$ scattering. At the intensity where Xe^{8+} ionization is 90%, the maximum $3.2 U_p$ return energies of 116 Hartree probe deep into the Xe^{8+} screened potential experiencing effective charges in the range of $rV(r) \approx 30$. The screening potential used for Ne^+ , He^+ , Ar^{8+} , and Ne^{8+} are shown in Fig. 2(d). As is well known, potentials are most accurately known for neutrals and single charge ions where experimental measurements have been done. The Ne^{8+} , Ar^{8+} , and Xe^{8+} ion potentials shown in Fig. 2(b,d) are sufficiently accurate for this work. Scattering is calculated for all ϕ and for θ between 0.05 to π radian forward to backscattering, respectively. An example of the angle and energy resolved scattering is shown in Fig. 2(c). The angle and energy integrated result from Fig. 2(c) is the total elastic scattering, which expressed as a ratio of the scattering / ionization is 2×10^{-4} for the example in Fig. 2(c).

III. RESULTS

A. Total Elastic Scattering

To determine the intensity dependence for angle and energy integrated scattering, we calculated the total elastic scattering for multiple species from 10^{15} to 10^{19} W/cm². Let us first direct attention to hydrogen-like species. These are the simplest to interpret as a

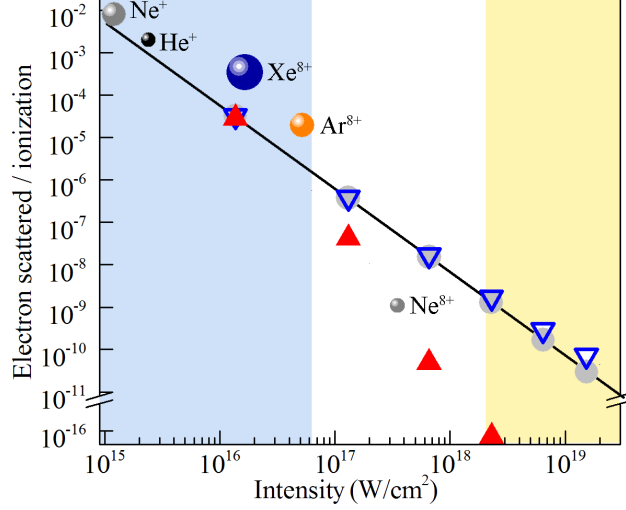


FIG. 3. (color online) Ratio of total scattered photoionization (all angles, energies greater than $0.3 U_p$) to photoionization as a function of intensity for hydrogen-like species with a non-relativistic dipole response with $2 \leq Z \leq 7$ (circle, gray), relativistic dipole response with $2 \leq Z \leq 7$ (inverted triangle, blue), and relativistic full E, B field response with $2 \leq Z \leq 5$ (filled triangle, red). A $1/I^2$ line (solid, black) is added. Noble gas scattering (sphere) is shown for Ne^+ (gray), He^+ (small, black), Xe^{8+} (large, blue), Ar^{8+} (orange), and Ne^{8+} (small, gray). Two regions are highlighted for $\Gamma_r < 1$ (light blue) and $a_0 > 1$ (light orange).

function of intensity, I , since a single parameter (Z) is changed as ionization proceeds from $Z = 2$ at 1.4×10^{16} W/cm² to $Z = 7$ at 1.6×10^{19} W/cm². Three different calculations are shown for the ionization, first is the non-relativistic case where the laser field is treated in the dipole approximation ($B = 0$). The calculated electron scattering as a fraction of the total ionization at the end of the laser pulse decreases from 10^{-2} in a 10^{15} W/cm² strong field to 10^{-11} in the ultrastrong field at 10^{19} W/cm². This tremendous reduction in the rescattering efficiency is consistent with the energy scaling in Rutherford scattering. A I^{-2} fit shown in Fig. 3 is in excellent agreement with the nonrelativistic, $B = 0$ case, due to a nonrelativistic recollision energy U_p that is linear in intensity. Second, we calculated the rescattering including relativistic effects in the continuum dynamics while maintaining the dipole approximation, i.e. $B = 0$. The results are similar to the non-relativistic calculations but there is an increase by a factor of 3 at 2×10^{19} W/cm² due to the relativistic mass shift limiting the excursion. The onset of the relativistic enhancement effects coincide with a classical field nonlinearity parameter $a_0 > 1$. Finally we included the full interaction with

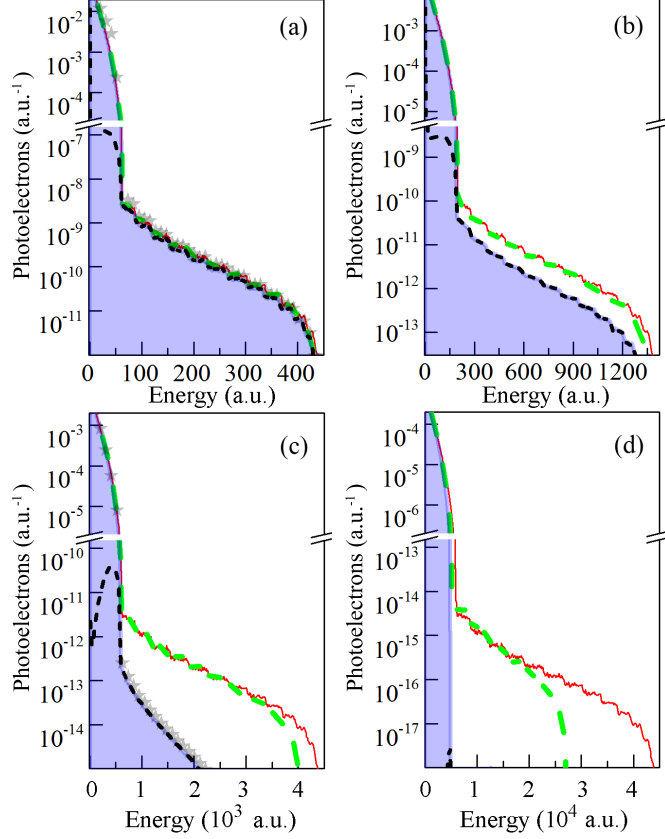


FIG. 4. (color online) Photoelectron energy spectrum for hydrogen-like species with a non-relativistic dipole response (thin, red), relativistic dipole response (dash, green), and relativity with B (filled, blue) at 2×10^{16} W/cm² (a), 6.3×10^{16} W/cm² (b), 2×10^{17} W/cm² (c), and 2×10^{18} W/cm² (d). The scattering component is shown (dotted, dark blue). To aid in (a-d) comparison the energy scale is 0 to $10.5 U_p$. The results when including Coulomb focusing (gray star symbol) for the full field, relativistic calculation are shown in (a) and (c).

relativity and B . The results follow closely the non-relativistic and relativistic cases until 6×10^{16} W/cm² where scattering begins to drop. By 2×10^{17} W/cm² the scattering is an order of magnitude smaller than the $1/I^2$ scaling. When the intensity reaches the value of $a_0 = 1$ at 2×10^{18} W/cm² the yield is reduced by seven orders of magnitude. This reduction in the scattering is due to the Lorentz deflection (Fig. 1) from B [20, 42] and consistent with the relativistic rescattering parameter, $\Gamma_r > 1$. The regime where Γ_r is much less than one may be considered in the nonrelativistic, $B = 0$ limit.

Included in Fig. 3 is scattering for noble gas ions with relativity and B . For clarity, these data points are labeled in the graph. As is indicated in Fig. 2(b), a screened potential

gives greater scattering. With scattering scaling as Z^2 , the yield from an atom such as xenon can be significantly greater than a bare nucleus of the same ion charge. We begin with traditional strong field ionization of the first charge state for Ne^+ (1×10^{15} W/cm², $U_p = 2.2$ a.u.) and He^+ (2×10^{15} W/cm², $U_p = 4.4$ a.u.). The calculated total scattering is within a factor of two times the hydrogen-like result for the Ne^+ scattering, due to the low scattering energy. The calculated scattering for He^+ is near the hydrogen-like results as well, due in addition to the small nuclear charge of two. Next we examine the scattering from Xe^{8+} (2×10^{16} W/cm²) and Ar^{8+} (5×10^{16} W/cm²). The scattering yield for Xe^{8+} and Ar^{8+} is an order of magnitude larger than the simple Hydrogen-like, Coulomb ion result due to the large screened nuclear charge. Both are at $\Gamma_r < 1$ intensities. Last is an excellent test case for scattering in ultrastrong fields. Ne^{8+} at 3×10^{17} W/cm² has photoelectron energies on the order of $U_p = 660$ a.u. With $\Gamma_r = 15.6$, the rescattering is expected to be strongly affected by B . Looking to Fig. 3 we can see the amount of scattering for Ne^{8+} is 60 times smaller than the non-relativistic, $B = 0$ hydrogen-like case and greater than the expected relativistic hydrogen-like case with B . A result consistent with a reduction from the Lorentz deflection and slight enhancement from a screened nuclear charge of ten. Experiments are underway to verify the drastic reduction in rescattering by nine orders of magnitude over an intensity change of only a factor of six.

B. Photoelectron Energy Spectra

Elastically scattered electrons are critical to understanding photoelectron final states. The maximum energy without scattering is $2 U_p$ while with scattering energies [43] can reach $10 U_p$. We begin the analysis of the photoelectron final energies for the three cases used previously: a traditional nonrelativistic strong field analysis with $B = 0$, including relativistic effects while setting $B = 0$, and the full field with relativistic dynamics. We begin in Fig. 4 with hydrogen-like ions and the portion of the spectrum resulting from elastic scattering with the parent ion at 2×10^{16} W/cm² ($\Gamma_r = 0.14, a_0 = 0.1$), 6×10^{16} W/cm² ($\Gamma_r = 0.94, a_0 = 0.17$), 2×10^{17} W/cm² ($\Gamma_r = 6.54, a_0 = 0.31$), and 2×10^{18} W/cm² ($\Gamma_r = 311, a_0 = 0.97$).

As we progress from Fig. 4(a) to Fig. 4(d) we see the evolution of the spectra and the impact of relativity and the Lorentz deflection. The agreement between all cases (Fig.

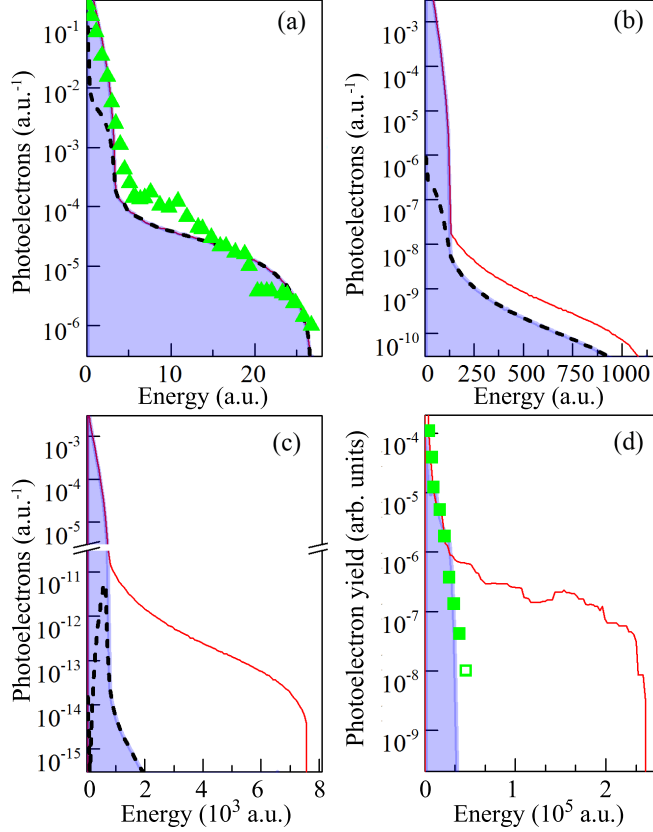


FIG. 5. (color online) Energy resolved photoelectron spectrum for Ne^+ (a), Ar^{8+} (b), Ne^{8+} (c), Xe^+ to Xe^{26+} (d) and a nonrelativistic dipole (thin, red), relativistic, E , B response (filled, blue) with the partial yield from rescattering (dotted, dark blue). Experimental data is shown (triangle) [43] and (square) [45]. For (d) the nonrelativistic response (thin, red) has been multiplied by 120 from the calculated value (dotted, red) to compare with the data. The open square data point in (d) is the limit of the signal to noise for that experimental energy.

4(a)) is consistent with a nonrelativistic, dipole interaction. With increasing intensity, the overall decrease in the contribution of elastic scattering to the photoelectron final state energy spectrum is quantified in Fig. 4(b) for a $\Gamma_r = 0.94$ where scattering is beginning to be suppressed as B deflects the returning electron. By the intensity of $2 \times 10^{17} \text{ W/cm}^2$, $\Gamma_r = 6.54$ in Fig. 4(c) nearly all elastic scattering has been suppressed with the highest energy photoelectrons most strongly affected. Finally, at $a_0 = 1$ in Fig. 4(d) one may infer that elastic scattering in the ultrastrong field does not occur, or at least is not observable at the level of 10^{-18} electrons per Hartree and steradian. For the sake of completeness we also show the spectra without the Lorentz deflection but including the relativistic mass shift.

The effect of relativistic continuum dynamics is to decrease the maximum kinetic energies attained from the field and elastic scattering.

Where the excursion of the electron is comparable to the ion potential, the force from the ion can affect the photoelectron in the continuum in a process known as Coulomb focusing [44]. One might at first suppose the large parent ion charges in ultrastrong fields could lead to strong Coulomb focussing effects. However, due to the large excursion that places the photoelectron far away from the parent ion and the high momentum gained from acceleration in the external field, Coulomb focusing plays a smaller role in ultrastrong fields. The Fig. 4(a,c) results have included the Coulomb focusing with the soft core potential described in Eq. 1-3. The increase in the rescattering can be seen in Fig. 4 but is only a fraction of the displayed symbol size.

Our last calculation is for noble gases, relativistically with full E , B fields and the scattering potentials described in Fig. 2. This work is intended to help bridge the gap between theoretical work and experimental efforts to quantify new ultrastrong field physics. To begin we connect to earlier, nonrelativistic strong field observations. Experimental data [43] is plotted in Fig. 5(a) along with our results for Ne^+ . Our calculations are consistent with the well-known strong field response and previous results [43]. In Figure 5(b) the photoelectron energy spectrum for Ar^{8+} is shown. With a $\Gamma_r = 0.87$, Ar^{8+} is beginning to be effected by B . The scattering reduction seen in Fig. 5(b) is consistent with the Lorentz rescattering parameter factor of $\exp(-\Gamma_r)$. In Fig. 5(c) the Ne^{8+} calculation reveals at $3 \times 10^{17} \text{ W/cm}^2$ for $\Gamma_r = 15.6$, scattering may be neglected since its occurrence is at the level of 10^{-14} electron per Hartree and steradian). The highest intensity presented is $1.2 \times 10^{19} \text{ W/cm}^2$ for the ionization of Xe at $\Gamma_r = 7, 480$, $a_0 = 2.4$. To compare with experiments, Fig. 5(d) has been modeled using the experimental focus, spatial volume, energy resolution, angular acceptance [17, 45], and multiple charge state distribution expected as ionization proceeds from neutral Xe to Xe^{26+} by the end of the pulse. Comparing the data with our calculation, one can see the high energy rescattering expected nonrelativistically is absent.

IV. CONCLUSION

A three-step model is extended into the relativistic, ultrastrong field regime ($\Gamma_r > 1$ and $a_0 < 10$). Continuum dynamics are treated semi-classically with Monte-Carlo trajectory en-

sembles to account for relativistic and B effects while ionization and rescattering is treated quantum mechanically. Studies of scattering in hydrogen-like systems show elastic rescattering generally obeys a $1/I^2$ scaling when the Lorentz deflection is small, i.e. $\Gamma_r < 1$. Elastic scattering decreases roughly as a function of $\exp(-\Gamma_r)$ until becoming undetectable. Relativistic mass effects are noted but play a smaller role, contributing for intensities beyond 10^{18} W/cm². In addition to work with fundamental hydrogen-like species, we calculated how the elastic scattering would be observed for noble gas species with screened atomic potentials. The results compare favorably with experimental data.

ACKNOWLEDGMENTS

This material is based upon work supported by the Army Research Office under Award No. W911NF-09-1-0390 and the National Science Foundation under Award PHY-1307042.

-
- [1] L. F. DiMauro and P. Agostini, *ADVANCES IN ATOMIC MOLECULAR AND OPTICAL PHYSICS D* **35**, 79 (1995).
 - [2] Y. Huismans, A. Rouzee, A. Gijsbertsen, J. H. Jungmann, A. S. Smolkowska, P. S. W. M. Logman, F. Lepine, C. Cauchy, S. Zamith, T. Marchenko, J. M. Bakker, G. Berden, B. Redlich, A. F. G. van der Meer, H. G. Muller, W. Vermin, K. J. Schafer, M. Spanner, M. Y. Ivanov, O. Smirnova, D. Bauer, S. V. Popruzhenko, and M. J. J. Vrakking, *SCIENCE* **331**, 61 (2011).
 - [3] T. Weber, H. Giessen, M. Weckenbrock, G. Urbasch, A. Staudte, L. Spielberger, O. Jagutzki, V. Mergel, M. Vollmer, and R. Dorner, *NATURE* **405**, 658 (2000).
 - [4] M.-C. Chen, C. Mancuso, C. Hernandez-Garcia, F. Dollar, B. Galloway, D. Popmintchev, P.-C. Huang, B. Walker, L. Plaja, A. A. Jaron-Becker, A. Becker, M. M. Murnane, H. C. Kapteyn, and T. Popmintchev, *PROCEEDINGS OF THE NATIONAL ACADEMY OF SCIENCES OF THE UNITED STATES OF AMERICA* **111**, E2361 (2014).
 - [5] J. Itatani, J. Levesque, D. Zeidler, H. Niikura, H. Pepin, J. Kieffer, P. Corkum, and D. Villeneuve, *NATURE* **432**, 867 (2004).
 - [6] D. B. Milosevic, G. G. Paulus, D. Bauer, and W. Becker, *JOURNAL OF PHYSICS B-ATOMIC MOLECULAR AND OPTICAL PHYSICS* **39**, R203 (2006).

- [7] A. LHuillier, K. Schafer, and K. Kulander, JOURNAL OF PHYSICS B-ATOMIC MOLECULAR AND OPTICAL PHYSICS **24**, 3315 (1991).
- [8] K. Burnett, V. Reed, and P. Knight, JOURNAL OF PHYSICS B-ATOMIC MOLECULAR AND OPTICAL PHYSICS **26**, 561 (1993).
- [9] A. Becker and F. Faisal, JOURNAL OF PHYSICS B-ATOMIC MOLECULAR AND OPTICAL PHYSICS **38**, R1 (2005).
- [10] V. Popov, PHYSICS-USPEKHI **47**, 855 (2004).
- [11] P. Lambropoulos, P. Maragakis, and J. Zhang, PHYSICS REPORTS-REVIEW SECTION OF PHYSICS LETTERS **305**, 203 (1998).
- [12] H. van der Hart, B. Doherty, J. Parker, and K. Taylor, JOURNAL OF PHYSICS B-ATOMIC MOLECULAR AND OPTICAL PHYSICS **38**, L207 (2005).
- [13] J. Parker, L. Moore, D. Dundas, and K. Taylor, JOURNAL OF PHYSICS B-ATOMIC MOLECULAR AND OPTICAL PHYSICS **33**, L691 (2000).
- [14] A. Kamor, C. Chandre, T. Uzer, and F. Mauger, PHYSICAL REVIEW LETTERS **112** (2014), 10.1103/PhysRevLett.112.133003.
- [15] W. Liu, J. Eberly, S. Haan, and R. Grobe, PHYSICAL REVIEW LETTERS **83**, 520 (1999).
- [16] P. Ho, R. Panfili, S. Haan, and J. Eberly, PHYSICAL REVIEW LETTERS **94** (2005), 10.1103/PhysRevLett.94.093002.
- [17] N. Ekanayake, S. Luo, P. D. Grugan, W. B. Crosby, A. D. Camilo, C. V. McCowan, R. Scalzi, A. Tramontozzi, L. E. Howard, S. J. Wells, C. Mancuso, T. Stanev, M. F. Decamp, and B. C. Walker, PHYSICAL REVIEW LETTERS **110** (2013), 10.1103/PhysRevLett.110.203003.
- [18] A. Di Piazza, C. Mueller, K. Z. Hatsagortsyan, and C. H. Keitel, REVIEWS OF MODERN PHYSICS **84**, 1177 (2012).
- [19] A. D. DiChiara, I. Ghebregziabher, R. Sauer, J. Waesche, S. Palaniyappan, B. L. Wen, and B. C. Walker, PHYSICAL REVIEW LETTERS **101** (2008), 10.1103/PhysRevLett.101.173002.
- [20] M. Walser, C. Keitel, A. Scrinzi, and T. Brabec, PHYSICAL REVIEW LETTERS **85**, 5082 (2000).
- [21] M. Chini, K. Zhao, and Z. Chang, NATURE PHOTONICS **8**, 178 (2014).
- [22] H. Bauke, H. G. Hetzheim, G. R. Mocken, M. Ruf, and C. H. Keitel, PHYSICAL REVIEW A **83** (2011), 10.1103/PhysRevA.83.063414.

- [23] S. S. Luo, P. D. Grugan, and B. C. Walker, JOURNAL OF PHYSICS B-ATOMIC MOLECULAR AND OPTICAL PHYSICS **47** (2014), 10.1088/0953-4075/47/13/135601.
- [24] P. D. Grugan, S. Luo, M. Videtto, C. Mancuso, and B. C. Walker, PHYSICAL REVIEW A **85** (2012), 10.1103/PhysRevA.85.053407.
- [25] S. X. Hu and A. F. Starace, PHYSICAL REVIEW E **73** (2006), 10.1103/PhysRevE.73.066502.
- [26] A. Maltsev and T. Ditmire, PHYSICAL REVIEW LETTERS **90** (2003), 10.1103/PhysRevLett.90.053002.
- [27] M. Klaiber, E. Yakaboylu, C. Mueller, H. Bauke, G. G. Paulus, and K. Z. Hatsagortsyan, JOURNAL OF PHYSICS B-ATOMIC MOLECULAR AND OPTICAL PHYSICS **47** (2014), 10.1088/0953-4075/47/6/065603.
- [28] V. Popov, PHYSICS-USPEKHI **47**, 855 (2004).
- [29] J.-X. Li, K. Z. Hatsagortsyan, and C. H. Keitel, PHYSICAL REVIEW LETTERS **113** (2014), 10.1103/PhysRevLett.113.044801.
- [30] P. Corkum, PHYSICAL REVIEW LETTERS **71**, 1994 (1993).
- [31] N. Ekanayake, S. Luo, P. D. Grugan, W. B. Crosby, A. D. Camilo, C. V. McCowan, R. Scalzi, A. Tramontozzi, L. E. Howard, S. J. Wells, C. Mancuso, T. Stanev, M. F. Decamp, and B. C. Walker, PHYSICAL REVIEW LETTERS **110** (2013), 10.1103/PhysRevLett.110.203003.
- [32] P. D. Grugan, S. Luo, M. Videtto, C. Mancuso, and B. C. Walker, PHYSICAL REVIEW A **85** (2012), 10.1103/PhysRevA.85.053407.
- [33] S. S. Luo, P. D. Grugan, and B. C. Walker, JOURNAL OF PHYSICS B-ATOMIC MOLECULAR AND OPTICAL PHYSICS **47** (2014), 10.1088/0953-4075/47/13/135601.
- [34] M. Klaiber, E. Yakaboylu, H. Bauke, K. Z. Hatsagortsyan, and C. H. Keitel, PHYSICAL REVIEW LETTERS **110** (2013), 10.1103/PhysRevLett.110.153004.
- [35] B. Walker, B. Sheehy, K. Kulander, and L. DiMauro, PHYSICAL REVIEW LETTERS **77**, 5031 (1996).
- [36] A.-T. Le, R. R. Lucchese, S. Tonzani, T. Morishita, and C. D. Lin, PHYSICAL REVIEW A **80** (2009), 10.1103/PhysRevA.80.013401.
- [37] S. Palaniyappan, I. Ghebregziabher, A. DiChiara, J. MacDonald, and B. C. Walker, PHYSICAL REVIEW A **74** (2006), 10.1103/PhysRevA.74.033403.
- [38] G. V. Dunne, EUROPEAN PHYSICAL JOURNAL D **55**, 327 (2009).

- [39] M. Ammosov, N. Delone, and V. Krainov, *ZHURNAL EKSPERIMENTALNOI I TEORETICHESKOI FIZIKI* **91**, 2008 (1986).
- [40] M. Klaiber, E. Yakaboylu, and K. Z. Hatsagortsyan, *PHYSICAL REVIEW A* **87** (2013), 10.1103/PhysRevA.87.023418.
- [41] F. Salvat, A. Jablonski, and C. Powell, *COMPUTER PHYSICS COMMUNICATIONS* **165**, 157 (2005).
- [42] C. Chirila, C. Joachain, N. Kylstra, and R. Potvliege, *PHYSICAL REVIEW LETTERS* **93** (2004), 10.1103/PhysRevLett.93.243603.
- [43] B. Sheehy, R. Lafon, M. Widmer, B. Walker, L. DiMauro, P. Agostini, and K. Kulander, *PHYSICAL REVIEW A* **58**, 3942 (1998).
- [44] D. Shafir, H. Soifer, C. Vozzi, A. S. Johnson, A. Hartung, Z. Dube, D. M. Villeneuve, P. B. Corkum, N. Dudovich, and A. Staudte, *PHYSICAL REVIEW LETTERS* **111** (2013), 10.1103/PhysRevLett.111.023005.
- [45] A. D. DiChiara, I. Ghebregziabher, J. M. Waesche, T. Stanev, N. Ekanayake, L. R. Barclay, S. J. Wells, A. Watts, M. Videtto, C. A. Mancuso, and B. C. Walker, *PHYSICAL REVIEW A* **81** (2010), 10.1103/PhysRevA.81.043417.